PAPERS | FEBRUARY 01 2026

From pinhole imaging to planetary orbit: A year-long solar angular measurement with a pinhole camera

Johannes Grebe-Ellis ; Thomas Quick

Am. J. Phys. 94, 106–112 (2026)
https://doi.org/10.1119/5.0289306

From pinhole imaging to planetary orbit: A year-long solar angular measurement with a pinhole camera

Johannes Grebe-Ellis[a)] and Thomas Quick[b)]
School of Mathematics and Natural Sciences, University of Wuppertal, Gaußstr. 20, 42119 Wuppertal, Germany

(Received 7 July 2025; accepted 17 November 2025)

We present a year-long experiment using a pinhole camera to determine the Sun's angular size, employing a flat mirror to project large-scale solar images of about 50–60 cm in diameter. Our analysis resolves the annual angular variation of 65 arc sec, reflecting Earth's elliptical orbit. Additionally, we observed atmospheric seeing effects (the effects of atmospheric turbulence) and sunspots visible with the naked eye. The project offers an accessible platform for high school and undergraduate students to engage in scientific inquiry.
https://doi.org/10.1119/5.0289306

I. INTRODUCTION

Pinhole images of the Sun are a common phenomenon in everyday life, often observed when sunlight filters through tree leaves or small gaps in blinds, producing circular or elliptical patches of light (Fig. 1). The phenomenon, known as "Sun coins," provides an accessible introduction to pinhole imaging in optical education. The diameter h of a solar pinhole image is determined by the Sun's angular extent θ and the imaging distance b. Given the Sun's mean angular diameter of 0.533° ($\approx 0.009\,30$ rad), the ratio $\theta = h/b \approx 1/108$ follows, meaning that the image diameter is approximately $1/108$ of the projection distance. However, due to the finite size of the pinhole aperture, which causes blurring and thus additional broadening of the image (optical convolution), a more practical approximation is the 1:100-rule: For every meter of projection distance, the Sun's image diameter increases by roughly 1 cm.

Due to the slightly elliptical orbit of Earth, the apparent diameter of the Sun varies over the course of a year, influencing the size of solar pinhole images. At *perihelion* (January 4), the solar angle θ reaches approximately $\theta_P \approx 0.542^\circ$ ($=32'33'' = 1953$ arc sec), while at *aphelion* (July 4), it decreases to about $\theta_A \approx 0.524^\circ$ ($=31'28'' = 1888$ arc sec). The difference of $\Delta\theta \approx 0.018^\circ$ ($=65$ arc sec) corresponds to a 3.4% variation relative to the mean value of 0.533° ($=1920$ arc sec). This fluctuation in the size of the solar image is subtle at short projection distances but becomes measurable at larger distances. For example, a projection distance of $b = 10$ m leads to an image size of about $h = 10$ cm and thus to a size fluctuation of $\Delta h \approx 3$ mm; at $b = 60$ m and an image size of about $h = 60$ cm, $\Delta h \approx 20$ mm. In this study, we present a year-long measurement of the annual size variation of large solar pinhole images, using simple methods suitable for educational purposes.

Historically, there has been a close connection between the measurement of the Sun's angle using pinhole cameras and the development of geometric optics, dating back to the 16th century and the work of Johannes Kepler.[1,2*]

However, as an astronomical instrument, the pinhole camera was soon replaced by the invention of the telescope. By the late 19th century, with Fraunhofer's invention of the heliometer, it became possible to measure the Sun's diameter with such precision that even physical fluctuations in the solar radius due to solar activity could be tracked over time.[4] In educational contexts, pinhole cameras and projectors are still widely used for solar observations, e.g., for projecting the solar disk or safely observing solar eclipses.[5,6] Numerous resources are available for the construction of simple pinhole projectors using index cards, cardboard boxes, or even disco balls.[7] In more advanced or professional settings, the use of pinhole cameras for quantitative solar measurements has also been explored. A notable approach comes from Sigismondi, who proposed using two pinholes instead of one.[8] By aligning the two resulting light cones, he derived a method to determine the apparent size of the Sun's image. To extend the projection distance and improve accuracy, he used a flat mirror,[9] a concept we also apply. However, to our knowledge, no measurements with the double-cone system have been published to date.

The structure of this paper is as follows. In the second section, we describe the annual variation of the solar angle based on astronomical principles. The third section presents the description of the solar pinhole image and specifies the geometric and diffraction-related influence of the imaging aperture. We demonstrate the conditions under which

*Kepler used pinhole cameras to measure the size of the solar disk.[3] His largest device had an image distance of almost 4 m, allowing him to project solar pinhole images with a diameter of $h \approx 40$ mm. The difference in size between the winter Sun image and the summer Sun image was therefore on the order of $\Delta h = 1.3$ mm. According to his records, Kepler nevertheless succeeded in resolving the annual variation in the solar angle: "But it is a certain thing, and evident to anyone to investigate, that the Sun's diameter at apogee is 30′, at perigee 31′."[3] Reconstructions of his measurements seem to confirm this, even though Kepler's measurement uncertainty was on the order of two arc minutes, respectively, $\delta h = h\,\delta\theta/\theta \approx 3$ mm.[1]

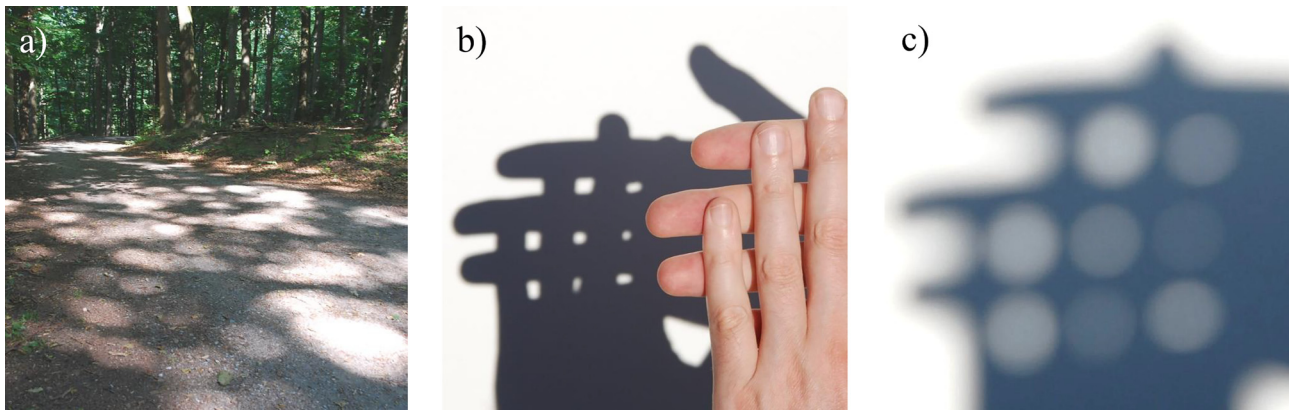

Fig. 1. Solar images on the ground under high leaf canopies (a), and created in the shadow of crossed fingers on a sunlit wall (b) and (c). Photos (b) and (c) Laila Ellis.

measurements can be interpreted using the ideal pinhole camera theory to determine the solar angle. In the fourth section, we describe the experimental setup, provide observational guidelines, and discuss relevant sources of uncertainty. The final section presents our measurement results and compares them with theoretical predictions. From our data, we extract the Earth's orbital eccentricity.

II. ANNUAL VARIATION OF THE APPARENT SOLAR DIAMETER

The apparent angular diameter of the Sun exhibits an annual variation due to the elliptical shape of Earth's orbit. According to Kepler's first law, planetary orbits are ellipses with the Sun at one focus. Consequently, the Earth–Sun distance l fluctuates throughout the year, with a minimum at *perihelion* (January 4) and a maximum at *aphelion* (July 4). The shape of an elliptical orbit is characterized by the numerical eccentricity $\varepsilon = e/a$, where e is the distance between the center of the ellipse and one of its foci and a is the semi-major axis. In the case of the Earth, whose orbit deviates only very slightly from that of a perfect circle ($e = 0$), the numerical eccentricity is approximately $\varepsilon = 0.016\,71$. From Fig. 2, the apparent angular diameter θ of the Sun is given by

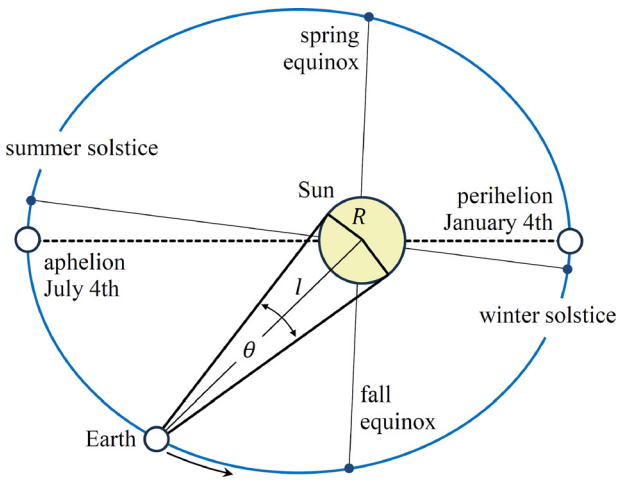

Fig. 2. Not-to-scale representation of the Earth's orbit with solar angle θ, Earth–Sun distance l and solar radius R.

$$\theta = 2\arcsin\left(\frac{R}{l}\right) \approx 2\frac{R}{l}, \tag{1}$$

where $R = 695\,700$ km is the physical radius of the Sun. The equation of the elliptical orbit with semi-major axis $a = 149.598\,022\,96 \times 10^6$ km and eccentricity ε is given by

$$l(\varphi) = \frac{a(1-\varepsilon^2)}{1+\varepsilon\cos\varphi}, \tag{2}$$

where φ is the so-called *true anomaly*, the angle between the perihelion and the current position of Earth as seen from the Sun.

For Earth's orbit, the eccentricity is small, so the Sun–Earth distance differs from the mean value a by only about $\pm 1.7\%$. The corresponding variation of the apparent solar diameter can therefore be described as a small periodic deviation from an almost constant value. By inserting the orbital distance $l(\varphi)$ from Eq. (2) into Eq. (1), the apparent angular diameter becomes

$$\theta(\varphi) \approx 2\,\frac{R}{l(\varphi)} = 2\,\frac{R}{a}\,\frac{1+\varepsilon\cos\varphi}{1-\varepsilon^2}. \tag{3}$$

Because $\varepsilon \ll 1$, the factor $1/(1-\varepsilon^2)$ differs from unity only marginally and may be neglected in a first-order treatment. This yields

$$\theta(\varphi) \approx \theta_0(1+\varepsilon\cos\varphi), \tag{4}$$

with $\theta_0 = 2R/a$. Equation (4) shows that the apparent diameter is largest at perihelion ($\varphi = 0$) and smallest at aphelion ($\varphi = \pi$). To express this variation as a function of time, we introduce the *mean anomaly* M, which increases uniformly with time. This is the angle that the Sun would make to perihelion if its orbit were circular. That is, with t_P equal to the time of perihelion and t the present time, then

$$M(t) = \frac{2\pi}{T}(t - t_{\mathrm{P}}), \tag{5}$$

where $T = 365.256$ d is Earth's orbital period. The true anomaly φ does not increase uniformly because the orbital speed varies along the ellipse. However, for the Earth's small eccentricity, the difference between φ and M leads only to terms of order ε^2 when used inside the cosine. It is therefore

sufficient in this context to replace $\cos\varphi$ by $\cos M(t)$. We thus obtain the time-dependent form given by

$$\theta(t) \approx \theta_0\left[1 + \varepsilon\cos\frac{2\pi}{T}(t - t_{\mathrm{P}})\right]. \tag{6}$$

The deviation between the first-order approximation in Eq. (6) and the curve obtained from the full elliptical theory is on the order of 1 arcsec over the course of the year.

III. THE SIZE OF THE SOLAR PINHOLE IMAGE: THEORETICAL PREDICTIONS

Imaging the Sun using a pinhole camera is an instructive experiment that demonstrates fundamental optical principles. It provides an intuitive means of understanding image formation without the use of lenses or mirrors. The total size h_{tot} of the solar pinhole image is essentially determined by the aperture geometry and the influence of diffraction. It is usually described by a twofold broadening of the ideal image h_{id} that theoretically results from a vanishing (infinitesimal) aperture,

$$h_{\mathrm{tot}} = h_{\mathrm{id}} + \delta_{\mathrm{geom}} + \delta_{\mathrm{diff}}, \tag{7}$$

with

$$h_{\mathrm{id}} = 2b\tan(\theta/2) \approx b\theta, \tag{8}$$

where θ describes the apparent size of the Sun (in radians) and b the image distance. The contribution $\delta_{\mathrm{geom}} = d$ takes into account the geometric influence of the finite aperture d imaging the effectively infinitely distant Sun. It illustrates that the solar image increases in size as the aperture enlarges and, therefore, highlights a fundamental trade-off in pinhole imaging: While a larger aperture increases irradiance, it reduces edge steepness due to convolution with the aperture. An optimal aperture size must be selected based on the intended application, balancing resolution and irradiance.

The term δ_{diff} reflects the additional broadening of the solar image due to diffraction. To specify δ_{diff}, we use the *Fresnel number* N_F to determine the diffraction regime in question. N_F is defined as $N_F = A/(\lambda b)$, where A is the aperture area, b is the image distance, and λ is the wavelength of light. For $10^{-2} \lesssim N_F \lesssim 10^2$, *Fresnel diffraction* dominates. This transitions to *Fraunhofer diffraction* for $N_F < 10^{-2}$ and to *geometrical optics* for $N_F > 100$.[10] Assuming an image distance of $b = 60$ m and a representative wavelength in the visible spectrum of $\lambda = 555 \times 10^{-9}$ m (maximum eye sensitivity), we find that for a circular aperture with $A = \pi d^2/4$, geometrical optics is valid for $d \gtrsim 65$ mm, while Fraunhofer diffraction applies for $d \lesssim 0.65$ mm. The apertures used in our experiments are in the range of 10–20 mm, placing the system entirely within the Fresnel regime.

Figure 3 shows the theoretical irradiance profiles of the solar image with the aforementioned contributions: the ideal projection, the geometric image, and the Fresnel-diffraction-corrected image (see the Appendix). The sharp geometric edge is smoothed into a more gradual transition due to diffraction, resulting in a slight but measurable increase in image size. To estimate this additional broadening δ_{diff} in Eq. (7), we consider the radius of the first Fresnel zone, $\sqrt{\lambda b}$, as a measure of the diffraction-induced blur. With regard to the image diameter, we obtain $\delta_{\mathrm{diff}} = 2\sqrt{\lambda b}$. The

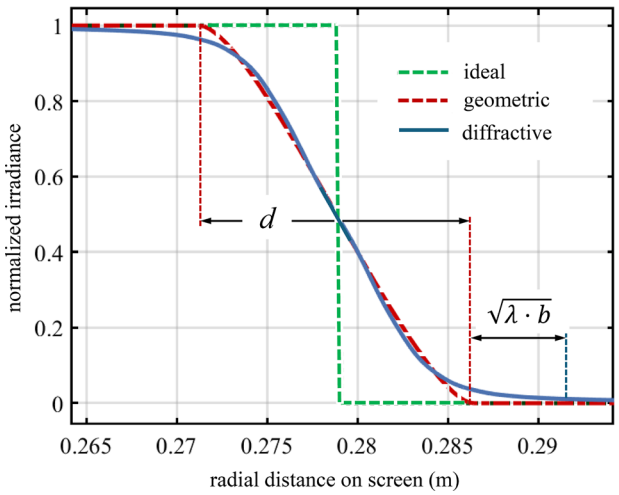

Fig. 3. Comparison of the irradiance profiles of the falling edge of the solar image h_{tot} based on the ideal, geometric, and diffraction-limited pinhole camera models. The curves intersect approximately at half of the normalized irradiance. They were calculated using the following parameters: $b = 60$ m, $\theta = 0.533°$, $\lambda = 555$ nm, and $d = 15$ mm.

total image diameter, accounting for diffraction effects, is then approximated by

$$h_{\mathrm{tot}} \approx b\theta + d + 2\sqrt{\lambda b}. \tag{9}$$

Computations for the solar image diameter using the above parameters ($b = 60$ m, $d = 15$ mm, and $\lambda = 555$ nm) yielded $h_{\mathrm{id}} = 0.558$ m, $h_{\mathrm{id}} + \delta_{\mathrm{geom}} = 0.573$ m, and $h_{\mathrm{tot}} = 0.585$ m using a mean solar angular diameter of $\theta = 0.533° = 0.009\,30$ rad.

A comparison of the contributions in Fig. 3 reveals an important methodological insight: When the image diameter is defined as the distance between the half-maximum flanks of the irradiance profile, the differences between the models become negligible. This suggests that, for practical purposes, the images can be treated as ideal pinhole projections, even in the Fresnel regime. Based on this consideration, we chose relatively large apertures (10–20 mm) to improve image contrast while maintaining sufficient geometric accuracy.

IV. EXPERIMENTAL SETUP: DESIGN, ANALYSIS METHODS, AND UNCERTAINTY ASSESSMENT

Our setup for producing large pinhole images of the Sun was fairly simple, inexpensive, and easily suitable for projects ranging from middle school to the undergraduate level. The most challenging part was finding a 60 m projection distance, preferably facing south, in a room that could be well darkened and had a sufficiently low building height so that it would not obscure the low-lying daytime arcs of the winter Sun. The setup consisted of a three-point-mounted flat first-surface mirror (Ø 40 mm) and a self-made aperture holder into which various circular apertures made of aluminum, each with a fixed diameter, could be inserted [Fig. 4(a)]. By decoupling the aperture and the mirror, the aperture could be oriented perpendicular to the beam. For the solar images of this study, an aperture of $d = 15.0$ mm was used, with a diameter accuracy better than 0.1 mm. The solar image was projected through an open window into a shaded room [Figs. 4(b) and 4(c)] onto a mobile blackboard covered with graph

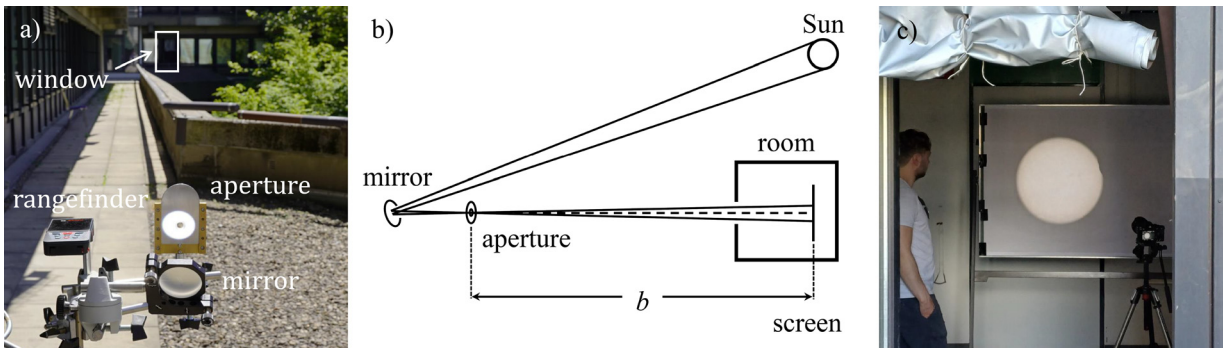

Fig. 4. Setup of the south-facing projecting path (a) and (b) and a closer look into the image room with a 55 cm solar image on the mobile blackboard covered with graph paper (c).

paper. The image distance b was measured with a laser rangefinder (Bosch GLM 150-27 C) with an accuracy of ± 1.5 mm. Mirror, aperture, and rangefinder formed a transportable setup placed on a mobile tripod for each measurement.

Before detailing the experimental procedure and the quantitative analysis, it is worth reporting some qualitative observations on large solar pinhole images. It is an awe-inspiring experience to observe the Sun in such a large, tangible way, making its dynamic nature and ever-changing surface features more accessible to the naked eye. The most obvious effect is the seeing, that is, the visual effects due to atmospheric turbulence: Wobbly striations swirl across the vibrating solar image, indicating the thermally driven air turbulence in the Earth's atmosphere and, of course, the rapid movement of the image, which moves approximately its diameter in 2 min. An unexpected and all the more fascinating phenomenon becomes visible at apertures of 15 mm and smaller, and thus with increasing image sharpness: dark sunspots, i.e., cooler regions of the solar surface that appear and disappear within several days and are caused by strong concentrations of magnetic flux (Fig. 5). Diffraction-related color fringes, which are expected, especially for very small apertures, were not observed. However, we observed the limb-darkening of the solar disk and a faint edge coloration, two effects of radiation transport that result from the Sun's spherical shape and are associated with a shift toward longer wavelengths.[11,12] The above observations already provide numerous starting points for classroom activities.

The main practical difficulty in measuring large-scale solar images is the rapid translation of the images. At a projection distance of 60 m, the image speed is about $0.5\,\mathrm{cm\,s^{-1}}$. With the mirror fixed in position, the horizontal window opening ($\sim$90 cm) limited the area on the board where the projected solar image could be observed to approximately two image diameters ($\sim$110 cm). To cope with this, we projected the image onto large-scale graph paper, took high-resolution photographs of it with a digital camera, and analyzed the irradiance profiles of these photos using the superimposed scale.

A measurement session was conducted by two people in phone contact: One adjusted the mirror and thus the image position, while the other provided instructions on the image position from the imaging room and took the photographs (with a webcam that transmits a live video of the screen, the experiment could also be carried out by one person). Each measurement session involved taking around 90 images with apertures of $d = 10$, 15, and 20 mm, i.e., 30 images per aperture. The aperture–screen distance was measured ten times. For the present analysis, we used only the 15 mm images, as this provided the best balance between the irradiance and the resolution determined by the aperture. Of the 30 images, the best ten were selected by visual inspection (low seeing, high sharpness, i.e., hardly any vibrations of the tripod due to wind or building vibrations).

To determine the image size, the free Image Analyzer software was used to create an irradiance profile of each image diameter along a narrow horizontal section (Fig. 6). The wavelength-resolved profiles generated from the RGB data of the photos showed a slight increase in the contribution of long wavelengths near the limb. For the evaluation, wavelength-averaged profiles integrated over the pixel columns were used. Following the theoretical prediction to identify the flank halves (Fig. 3), boxes of the aperture width d were placed on both flanks of the irradiance profile (Fig. 6). The distance between the medians of the boxes was then read as h_{id} with an accuracy of ± 1 mm, using the graph-paper scale visible in the profile. Combined with the

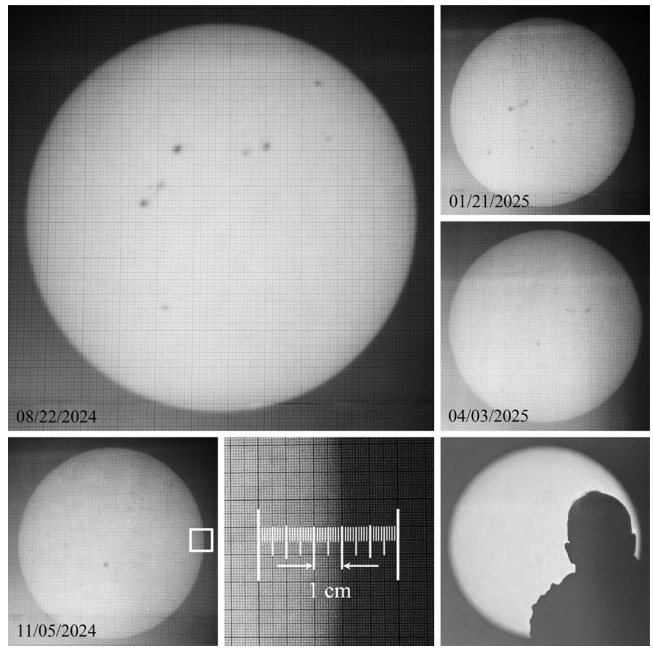

Fig. 5. Large pinhole images of the Sun, projected onto graph paper, showing the pattern of sunspots of the respective day. The image section marked at the bottom left is enlarged at the bottom center to make the lines on the graph paper visible, which are used to measure the image size.

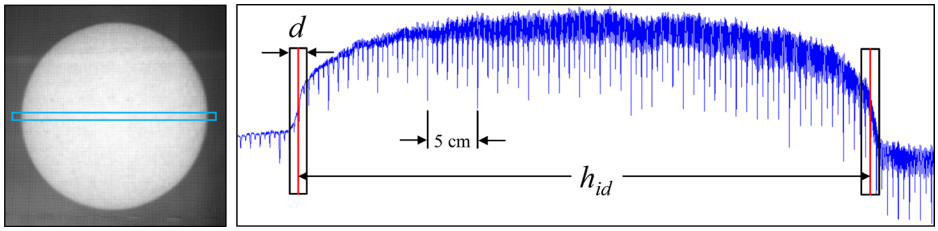

Fig. 6. In order to obtain the image size from the irradiance profile, both flanks were marked with boxes of aperture width d. Using the lines of the graph paper, which are clearly visible in the profile, the distance between the box medians was taken as h_{id}.

measured b, we used the relation $\theta = h_{\mathrm{id}}/b$ to directly derive the apparent solar diameter for the current day.

To estimate the uncertainty $\delta\theta$ of the measured solar angle θ, we considered both b and h_{id}: The distance b was measured ten times per date. The statistical uncertainty is negligible ($\delta b_{\mathrm{stat}} \approx \pm 0.2$ mm). The systematic contributions are treated as symmetric (sign-indeterminate) uncertainties and are combined in quadrature: 1. The rangefinder's specified uncertainty (± 1.5 mm) is included. 2. The beam hits the center of the screen perpendicularly but deviates slightly across the width of the screen (1.2 m) as the solar image moves (up to ± 2 mm at 60 m). 3. A small height mismatch between the pinhole and the rangefinder (estimated ± 2 mm) is taken into account. In quadrature, this yields $\delta b = \pm 3.2$ mm.

The image size h_{id} was visually assessed based on the respective irradiance profile by a person who had no knowledge of the theoretically expected solar angle on that day and who was not involved in the data analysis. The statistical uncertainty was calculated from the standard deviation of ten measurements and is typically $\delta h_{\mathrm{stat}} \approx \pm 0.3$ mm. Systematic contributions are as follows: 1. A 5° tilt between the screen and the aperture gives a geometric systematic uncertainty of 0.3% (about 1.8 mm for a 60 cm image). 2. Visual reading from a millimeter scale adds another 1 mm uncertainty. Combining these gives a total $\delta h_{id} = \pm 2.1$ mm.

From these contributions, the uncertainty in the solar angle is estimated to be $\delta\theta = \pm 8$ arcsec (i.e., $\pm 0.002°$ or ± 0.00004 rad). So, we use one significant digit for the uncertainty and apply this convention throughout the paper. Given a mean solar angle of $\theta = 1920$ arc sec, $\delta\theta = \pm 8$ arc sec corresponds to a relative uncertainty of approximately 0.4%. Over the course of a year, this accuracy is sufficient to detect seasonal variations in the apparent solar diameter.

V. EXPERIMENTAL RESULTS AND THEIR IMPLICATIONS FOR EARTH'S ORBIT

In this section, we present our measurements of the solar angular diameter collected between July 2024 and July 2025 (Table I) and compare them with the calculated values of the solar angle. From the fit of the measurements to the model, the eccentricity of the Earth's orbit can be directly derived. Figure 7 shows the theoretical curve, as derived in Sec. II, alongside 19 measured angular diameters determined using Eq. (8). Table 1 summarizes the measured angular diameters, the corresponding mean values of image distance and image size, and the theoretical predictions. The root-mean-square residual is RMS = 3.0 arc sec, and the coefficient of determination is $R^2 = 0.983$, indicating a good agreement between theory and observation.

Let θ_P and θ_A be the observed apparent solar angles at perihelion and aphelion. For small angles, the solar angle is inversely proportional to the Sun–Earth distance [Eq. (1)], while $l_P = l(0°) = a(1-\varepsilon)$ and $l_A = l(180°) = a(1+\varepsilon)$ [Eq. (2)]. We obtain

$$\frac{\theta_P}{\theta_A} = \frac{l_A}{l_P} = \frac{1+\varepsilon}{1-\varepsilon}. \tag{10}$$

This relation yields

$$\varepsilon = \frac{\theta_P - \theta_A}{\theta_P + \theta_A}. \tag{11}$$

Using our measured values $\theta_P = 1947$ arc sec in early January (01/13/2025) near perihelion and $\theta_A = 1883$ arc sec in early July (07/03/2025) near aphelion, our final result is $\varepsilon = 0.0167 \pm 0.0030$, which is in good agreement with the known eccentricity of Earth's orbit of 0.01671.

Our measurement provides another point which may be interesting for discussion with students: the question of empirical underdetermination of theories. Because Earth's orbital eccentricity is very small, the annual change in the apparent solar diameter is small and almost cosine-like; therefore, several descriptions fit the diameter series equally

Table I. Monthly measurements vs the calculated solar angle θ_{calc}. Uncertainties: $b = \pm 3.2$ mm, $h_{\mathrm{id}} = \pm 2.1$ mm, implying $\delta\theta = \pm 8$ arc sec (Fig. 7). Angles θ are computed from internally unrounded means; h_{id} is shown with two decimals to enable direct reproduction.

Nr	Date	t (days)	b (cm)	h_{id} (cm)	θ (arc sec)	θ_{calc} (arc sec)
1	07/15/24	197	5416.1	49.48	1884	1887
2	08/22/24	235	5872.1	54.03	1898	1897
3	09/16/24	260	5827.5	53.71	1903	1908
4	10/15/24	289	5805.7	54.18	1925	1924
5	11/05/24	310	5802.1	54.37	1933	1935
6	12/27/24	362	5830.1	55.00	1946	1951
7	01/13/25	13	5830.0	55.03	1947	1951
8	01/21/25	21	5817.9	54.95	1948	1950
9	02/03/25	34	5819.6	54.84	1944	1947
10	02/17/25	48	5998.4	56.36	1938	1942
11	03/06/25	65	5990.1	56.14	1934	1934
12	03/19/25	78	5993.0	56.06	1929	1927
13	04/03/25	93	5992.4	55.74	1919	1919
14	04/28/25	118	5982.6	55.39	1910	1906
15	05/09/25	129	5997.1	55.32	1903	1901
16	06/03/25	154	6187.8	56.79	1893	1892
17	06/12/25	163	6188.3	56.60	1885	1889
18	06/25/25	177	6186.9	56.56	1886	1887
19	07/03/25	182	6188.5	56.49	1883	1887

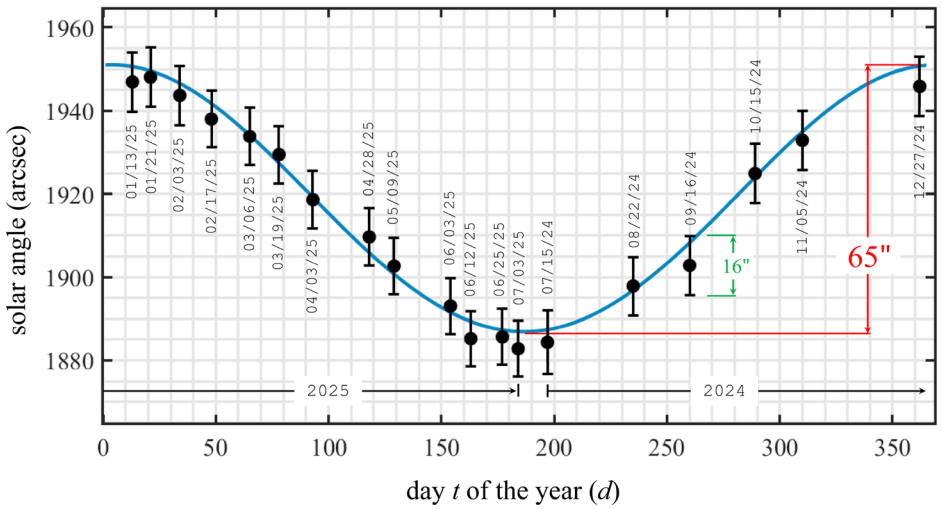

Fig. 7. The solar angle θ, determined on the basis of the data recorded between July 15, 2024 and July 3, 2025 compared with the calculated seasonal variation of θ.

well. First, there is the full Keplerian model, with an ellipse and the Earth–Sun distance determined from Kepler's laws. Second, there is our phenomenological description, which fits a cosine-like annual modulation with the observed amplitude and phase. Third, there is the historically earlier geometric model of an eccentric circle, used already in pre-Keplerian astronomy for the Sun's annual anomaly: The motion is circular and uniform, but the Sun is slightly displaced from the center, which also produces a small yearly change in the apparent solar size. This is a case of empirical underdetermination: With diameter data alone, all three descriptions remain compatible. To distinguish them, additional observations are needed that determine the law of time—i.e., how the position of the Sun actually changes over time (e.g., based on ecliptic longitude)—or independent distance information. Our approach is therefore confirmatory: We examine whether our data follow the expected curve.

VI. CONCLUSION

Observing an image of the Sun with a diameter of 55 cm up close with the naked eye is a thrilling experience. It offers an exciting series of observations that are relevant for teaching optics, astrophysics, and astronomy: The flickering and dancing of the image's schlieren (astronomical seeing as a problem of earthbound observation), the movement of the image, characteristic patterns of current sunspots, limb-darkening, and the coloration of the Sun's edges.

To reproduce the experiment described in a teaching context, it is useful to estimate the minimum projection distance required to resolve the annual variation $\Delta\theta = 65'' = 3.151 \times 10^{-4}$ rad. At $b = 50 - 60$ m, we obtain a signal-to-noise ratio of SNR $= \Delta\theta/(2\,\delta\theta) = 65''/16'' \approx 4.1$, which corresponds to a full uncertainty span of $2\,\delta h_{\mathrm{id}} \approx 4$ mm (i.e., $\delta h_{\mathrm{id}} \approx 2$ mm). We then ask how small b can be so that, under poorer SNR conditions (target SNR $= 3$ or 2), the span $2\,\delta h_{\mathrm{id}}$ does not exceed ≈ 4 mm. Using $\Delta h = b\,\Delta\theta$ and SNR $= \Delta h/(2\,\delta h_{\mathrm{id}})$, we obtain $b_{\min} = 2\mathrm{SNR}\delta h_{\mathrm{id}}/\Delta\theta$; this gives $b_{\min} \approx 38$ m for SNR $= 3$ and $b_{\min} \approx 25$ m for SNR $= 2$. Thus, with projection distances of about 20–40 m, the seasonal variation should be just resolvable.

Finally, we would like to highlight an interesting extension of our experimental approach that enables a test of Kepler's second law. This law states that the line connecting a planet to the Sun sweeps out equal areas in equal times. This implies $dA/dt = \frac{1}{2}l^2\dot{\varphi} = \mathrm{const}$. Since we obtain the Earth–Sun distance l from the apparent angular diameter of the Sun, the angular velocity $\dot{\varphi}$ must be derived independently. This can be done by tracking how the Sun's ecliptic longitude $\lambda_\odot$ changes over time, as each change corresponds directly to Earth's motion along its orbit.

Our year-long observations demonstrate how simple pinhole imaging can reveal insights about Earth's orbital motion—truly a journey from pinhole to planetary orbit.

ACKNOWLEDGMENTS

The authors thank the reviewers and the editor for valuable suggestions, which improved the clarity and presentation of this paper.

AUTHOR DECLARATIONS

Conflict of Interest

The authors have no conflicts to disclose.

APPENDIX: FRESNEL PROFILE OF A PINHOLE PROJECTION

The circular aperture is described by

$$A(x,y) = \begin{cases} 1, & x^2 + y^2 \le (d/2)^2, \\ 0 & \text{otherwise.} \end{cases} \tag{A1}$$

Propagation to the screen at distance b is carried out with the angular spectrum method. With wavenumber $k = 2\pi/\lambda$ and spatial frequencies (f_x, f_y), the transfer function is

$$H(f_x,f_y) = \exp\left[-i\pi\lambda b\,(f_x^2 + f_y^2)\right]. \tag{A2}$$

The propagated complex scalar field amplitude at the screen is

$$U_b(x,y) = \mathcal{F}^{-1}\{\mathcal{F}\{A\}(f_x,f_y)\,H(f_x,f_y)\}, \tag{A3}$$

and the normalized point-spread function is

$$E_{\mathrm{PSF}_\lambda}(x,y) = \frac{|U_b(x,y)|^2}{\max|U_b|^2}. \tag{A4}$$

This is the (relative) irradiance distribution on the screen for a monochromatic point source at wavelength λ. The solar disk is modeled as a uniform top-hat of radius $R = b\,\theta/2$ (constant source radiance assumed),

$$O(x,y) = \Pi\left(\frac{\sqrt{x^2+y^2}}{R}\right), \tag{A5}$$

and the (relative) irradiance of the image follows from the convolution

$$E_\lambda(x,y) = (O * E_{\mathrm{PSF}_\lambda})(x,y). \tag{A6}$$

The horizontal profile is $E_\lambda(x,0)$, normalized to unity.

[a]Electronic mail: grebe-ellis@uni-wuppertal.de, ORCID: 0000-0003-0400-0780.
[b]Electronic mail: quick@uni-wuppertal.de, ORCID: 0000-0002-9201-6231.

[1]C. Sigismondi and F. Fraschetti, "Measurements of the solar diameter at Kepler's time," Observatory **121**, 380–385 (2001).
[2]T. Quick and J. Grebe-Ellis, "Kepler's Moon puzzle—A historical context for pinhole imaging," Am. J. Phys. **93**(3), 215–222 (2025).
[3]J. Kepler, *Optics*, translated by William H. Donahue (Green Lion Press, Santa Fe, New Mexico, 2000), p. 353.
[4]C. Sigismondi, "Ground-based measurements solar diameter," arXiv:1106.2537 [astro-ph.SR] (2011).
[5]M. Young, "The pinhole camera: Imaging without lenses or mirrors," Phys. Teach. **27**(9), 648–655 (1989).
[6]J. A. Roberts, "Mapping the sun's path with a pinhole camera," Sci. Activities **32**(1), 24–27 (1995).
[7]Robert J. Cumming, Alexander G. M. Pietrow, Livia Pietrow, Maria Cavallius, Dominique Petit dit de la Roche, Casper Pietrow, Ilane Schroetter, and Moa Skan, "Why every observatory needs a disco ball," Phys. Educ. **59**(2), 025012 (2024).
[8]C. Sigismondi, "Measuring the angular solar diameter using two pinholes," Am. J. Phys. **70**(11), 1157–1159 (2002).
[9]T. H. Nilsson, "Pinhead mirror: a previously undiscovered imaging device?," Appl. Opt. **25**(17), 2863–2864 (1986).
[10]L. S. Pedrotti, F. L. Pedrotti, and L. M. Pedrotti, *Introduction to Optics* (Pearson, 2017).
[11]W. Suhr, "Gesiebtes Licht (sifted light)," Phys. Unserer Zeit **48**(5), 243–245 (2017).
[12]S. S. R. Inbanathan, K. Moorthy, and S. Ashok Kumar, "Observing solar limb darkening in the classroom," Phys. Teach **59**(4), 292–293 (2021).

Then I'll start work on my lunar engines to line the Moon up with the ecliptic so we can have a solar eclipse every month (with a little wobble so they're not always on the equator.) (Source: https://xkcd.com/2792)